11th International Symposium on Turbulence and Shear Flow Phenomena (TSFP11)
Southampton, UK, July 30 to August 2, 2019

TRANSITION TO TURBULENCE OF THE WAKE OF SUPER-HYDROPHOBIC SPHERES

Marco Castagna
PRISME Laboratory
University of Orléans
8, Rue Léonard De Vinci
45072, Orléans, France
marco.castagna@univ-orleans.fr

Nicolas Mazellier
PRISME Laboratory
University of Orléans
8, Rue Léonard De Vinci
45072, Orléans, France
nicolas.mazellier@univ-orleans.fr

Azeddine Kourta
PRISME Laboratory
University of Orléans
8, Rue Léonard De Vinci
45072, Orléans, France
azeddine.kourta@univ-orleans.fr

ABSTRACT

This work deals with an experimental investigation of free falling super-hydrophobic spheres in glycerol-water mixtures over a wide range of Reynolds number. The super-hydrophobic coatings have the ability, once in contact with a suitable liquid, to reduce the interaction area between the latter and the solid surface by entrapping an air layer in the surface roughness. We thus investigate a possible effect of this feature on the hydrodynamic performance of spheres, focusing our attention on the onset of wake instabilities. Surprisingly, the detected behaviour of the super-hydrophobic coatings depends on the analysed flow regime. A possible connection between the hydrodynamic performance and the deformation of the air layer encapsulating the coated spheres is proposed.

MOTIVATIONS

The presence of an air layer between a solid surface and a liquid interacting with it may be interesting for a large range of industrial applications, encompassing glasses for self-cleaning windows, retarding ice-growth rate surfaces, corrosion-resistant equipments and drag-reducing walls for liquids transport or moving objects (Zhang *et al.*, 2008). The air trapped among the roughness elements of super-hydrophobic (SH) surfaces may thus be beneficial in the framework of passive control methods for hydrodynamic performance amelioration of marine vehicles. A large number of studies (see e.g. the review by Ern *et al.* (2012)) investigated the role of parameters as body shape and boundary condition at the wall on the development of the wake of free falling/rising objects. However, the experimental works on SH falling spheres usually focused their attention on the terminal velocity V_∞, sometimes retrieving discordant results in terms of terminal drag. While the drag reducing capability of a sustained air layer in a terminal Reynolds number (Re_∞, based on V_∞ and sphere diameter d) regime corresponding to the drag crisis (see Fig. 1) is quite convincing (Vakarelski *et al.*, 2014), the few available results at lower Re_∞ evidenced both drag decrease (McHale *et al.*, 2009) and increase (Ahmmed *et al.*, 2016) or negligible effects (Byon *et al.*, 2010). A further step in the comprehension of the SH coatings behaviour was made by analysing the state of the air/liquid interface, showing that a deformation of the interface could lead to significant effects on the evaluated hydrodynamic performance (Song *et al.*, 2018).

In this framework, the present authors executed a large experimental campaign covering the Re_∞ ranges highlighted in Fig. 1. The high Re_∞ region was investigated in Castagna *et al.* (2018), where the interplay between the air/liquid interface deformation and the amount of vorticity produced at the sphere wall and then shed in the wake was underlined. The resulting influence on the hydrodynamic performance could lead both to drag reduction or increase depending on the relative deformation of the air layer. Moreover, the SH coatings were found to promote the onset of transversal motion of the falling sphere, that is the wake instabilities were triggered earlier. In the low Re_∞ regime, before the appearance of the transitions characterising the sphere wake (Jenny *et al.*, 2004), a negligible effect of randomly distributed SH coatings on the terminal drag of falling spheres was evaluated (Castagna *et al.*, 2019). This result was explained via a porous medium approach that took into account the detrimental effect on drag caused by the motion of the air among the surface roughness elements. The present paper thus focuses on the intermediate Re_∞ regime, which corresponds to the region were the wake of the sphere undergoes multiple transitions (see e.g. Jenny *et al.*, 2004, and discussion below).

The paper is organised as follows: the experimental set-up is described first, followed by a characterisation of the analysed SH coatings. Then, results sampled from the executed experimental campaign are presented and discussed.

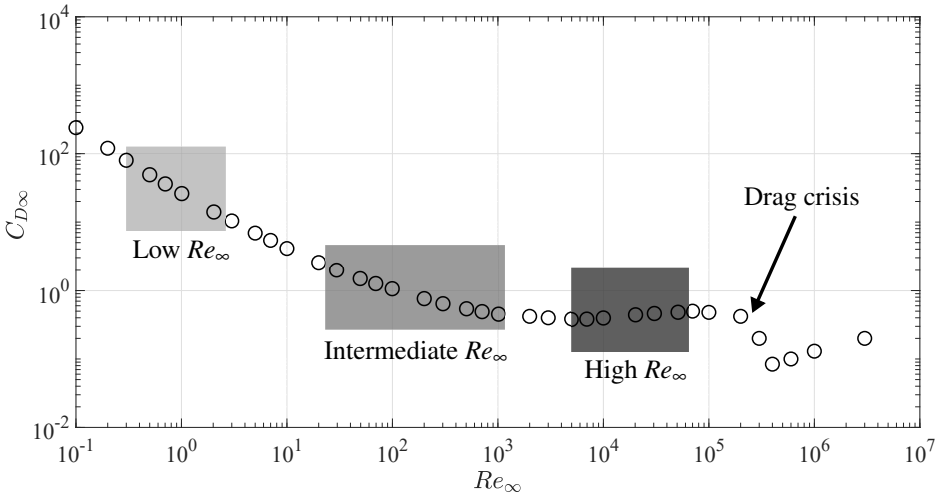

Figure 1: Terminal drag coefficient $C_{D\infty}$ as a function of the terminal Reynolds number Re_∞ for reference spheres. ○, experimental data from Lapple & Sheperd (1940). The grey-shaded rectangles indicate the whole Re_∞ range analysed with our falling spheres experiments. All the shown results lie below the appearance of the drag crisis phenomenon, indicated by the black arrow.

EXPERIMENTAL SET-UP

The falling sphere experiments were performed in a transparent vertical tank with a 100×100 mm^2 square cross-section and a 650 mm height (see Fig. 2). All tests were performed at room temperature equal to 20 ± 1 °C, which was verified by a thermocouple dipped in the liquid filling the tank. At the beginning of the test, the spheres were gently dipped below the liquid free surface by an electromagnetic holder. The latter was then used to control the release of the sphere, thus assuring a null initial velocity. The working fluid spanned from pure glycerol (low Re_∞ region in Fig. 1) to pure water (high Re_∞ region in Fig. 1). The intermediate Re_∞ was reached by varying the relative volumetric fraction of the two liquids in the glycerol-water mixtures. The properties of the latter are resumed in Tab. 1, together with information about the tests execution

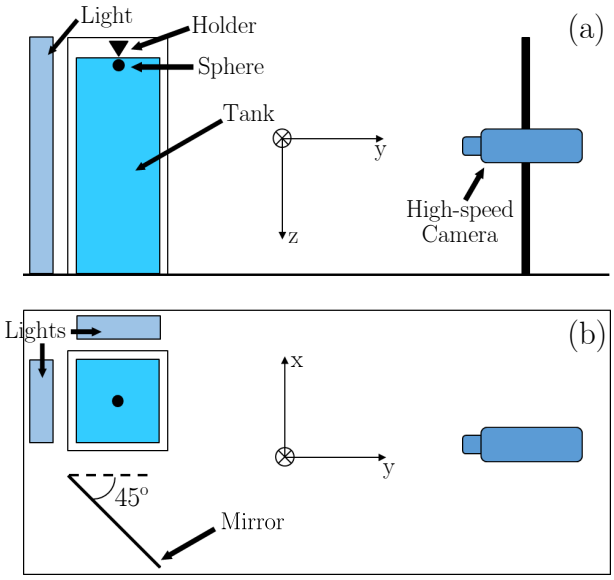

Figure 2: Schematic of the falling sphere experimental set-up. (a), side view. (b) top view.

and the analysed spheres. The diameter d of the reference stainless spheres varied in the range $5-25$ mm depending on the analysed mixture. The trajectory of the falling sphere was recorded by a Phantom V341 high-speed camera and the configuration resulted into a spatial resolution of 0.3 mm px^{-1}. The recording frame rate varied in the range $200-1000$ fps since it was adapted to the falling sphere velocity magnitude, which strongly varied depending on the considered mixture and sphere diameter. The transversal motion in the $z-y$ plane was made available by the presence of a mirror placed at 45° with respect to the tank side wall. The three-dimensional (3D) time-resolved displacement of the sphere was reconstructed by a cross-correlation code developed in MATLAB®. A sub-pixel accuracy of $\approx \pm$ 0.06 px, that is lower than 0.4% of the smallest analysed d, was achieved by a Gaussian fit of the correlation peak (Raffel *et al.*, 2007). The velocity profiles were obtained via the smoothing spline technique described in Epps & Truscott (2010). The evaluated V_∞ were in the range $0.07-2.50$ ms^{-1}, which correspond to a Re_∞ field $3.0\times10^{-1}-6.4\times10^4$. When necessary, the velocities were corrected for confinement effects due to the finite size of the tank cross-section following the technique proposed by Di Felice (1996):

$$\frac{V_\infty^{bou}}{V_\infty^{unb}} = \left(\frac{1-\delta}{1-0.33\delta}\right)^{\alpha} \tag{1}$$

where the ratio of the bounded terminal velocity V_∞^{bou} with respect to the unbounded V_∞^{unb} counterpart depends on the blockage factor $\delta = d/D_{tank}^{eq}$. In the latter expression, $D_{tank}^{eq} = 2l/\sqrt{\pi}$ (l being the tank width) is the equivalent diameter of the tank. Finally, the exponent α in eq. (1) was evaluated by the following expression (Di Felice, 1996):

$$\frac{3.3-\alpha}{\alpha-0.85} = 0.27 Re_\infty^{0.64} \tag{2}$$

Table 1: Nomenclature and properties of the glycerol-water mixtures investigated in the falling spheres experimental campaign, from pure water to pure glycerol. The water and glycerol percentages represent the volumetric fractions. The settling time indicates the minimum time required between two consecutive tests to assure the liquid to be quiescent. The number of executed tests per each sphere was a compromise between statistical relevance and duration of the experimental campaigns. The last column indicates the sphere diameter range investigated in each mixture.

Mixture Name	Water Fraction, [%]	Glycerol Fraction, [%]	Settling Time, [*min*]	Number of Tests	Diameter Range, [*mm*]
G000	100	0	15	10	5-25
G060	40	60	30	10	5-10
G070	30	70	30	10	5-10
G080	20	80	30	10	5-10
G100	0	100	60	5	5-10

COATINGS CHARACTERISATION

The SH spheres were produced by applying a SH coating over the reference stainless steel spheres via a spray method, using a commercially available SH painting (Ultra-Ever Dry®). The manufacturing procedure was explained in detail in Castagna *et al.* (2018). It consists in spraying an etch primer to create a suitable substrate, eventually enhancing the surface roughness by embedding a carbon-based powder with a suitable particles size d_p and finally spraying a top coating that assures the SH behaviour to be achieved. The coating without embedded powder as intermediate layer will be called SH-1. The two coatings with embedded powder will be indicated hereinafter as SH-2 ($d_p \approx 70\ \mu m$) and SH-3 ($d_p \approx 200\ \mu m$) in order of increasing root-mean-square surface roughness λ. The latter was evaluated by 3D digital microscopy measurements over SH flat plates (see Fig. 3), spanning a range $25-142\ \mu m$. The sequence in Fig. 3 highlights the modification of the surface texture for increasing powder particle size. In all cases, a random spatial distribution of the elements is obtained. The properties of the produced SH coatings are resumed in Tab. 2, for the two extreme cases of pure water (G000 mixture) and pure glycerol (G100 mixture). The static contact angle ϑ_s was evaluated via the sessile drop technique with a digital goniometer over SH flat plates. The slight ϑ_s average values decrease in the G100 mixture testifies the non-significant modification of the SH behaviour of the produced coatings with respect to the different liquids analysed in this study. No significant modifications of the roll-off angle ϑ_r (the lowest tilt angle of the flat plate that forces the drop to roll-off) are evaluated.

FALLING SPHERE RESULTS

An indication of the Re_∞ reached by the spheres in the intermediate glycerol-water mixtures is reported in Tab. 3. These data show that, varying the fractions of the two liquids and the sphere diameter, the ranges achieved with the different mixtures overlap. This choice was made to cover the Re_∞ regions where the sphere wake transitions happen (Jenny *et al.*, 2004). In fact, in the case of a fixed sphere, the axisymmetric wake characterising the low Re_∞ region is lost at $Re_\infty \approx 212$ in favour of a steady planar-symmetric wake. The latter becomes periodic at $Re_\infty \approx 275$, while losing the symmetry at $Re_\infty \approx 350$. A further Re_∞ increase leads to the so-called *chaotic* regime, where the characteristic frequency of the vortex shedding is no more clearly identifiable. The transitions mechanism was shown to keep qualitatively similar in the case of a free falling/rising sphere, highlighting the close relationship between wake and path instability (Ern *et al.*, 2012). Moreover, the critical Reynolds number at which path instability of a free body and wake instability of a fixed sphere occur were shown to be closely related.

Based on this picture, we show in Fig. 4 the normalised transversal velocity $V_{tr}^\star = \sqrt{V_x^2 + V_y^2}/V_0$ (see Fig. 2 for the coordinate system definition) of the $d = 10$ *mm* spheres for the mixture G080 and of the $d = 5$ *mm* spheres for the mixture G070, which reach $Re_\infty \approx 100$ (axisymmetric wake) as shown in Tab. 3. The time $t_0 = \sqrt{d/\left((\zeta-1)\,g\right)}$ (ζ being the ratio between sphere and liquid density) and the velocity $V_0 = \sqrt{(\zeta-1)\,gd}$ were chosen as scaling parameters to take into account gravity/buoyancy effects (Jenny *et al.*, 2004). A $V_{tr}^\star$ peak appears in both Figs. 4a and 4b in the SH-3 case, which is not detected in the reference sphere. However, the peak magnitude only reaches approximately four times the baseline value of the reference, testifying that in this Re_∞ range below the transitions region the effect of the SH coatings on the onset of the transversal motion is limited. Moreover, after the peak occurrence the $V_{tr}^\star$ approximately falls back to the reference case profile.

The scenario changes by analysing the velocity profiles of the spheres that lie, in terms of Re_∞, within and above the wake transitions region. The $V_{tr}^\star$ of the $d = 8$ *mm* spheres falling in the mixture G070 show a strong increase of the transversal motion starting from $t^\star \approx 10$ (see Fig. 5a). Interestingly, an increase of the λ value determines an earlier trigger of the transversal motion. Moreover, after the ascending part of the $V_{tr}^\star$ peak, the profiles do not come back to the departure value as in the cases shown in Fig. 4, and the magnitude reached is equal or larger than ten times the baseline value. A significant difference is noticed between the coatings with embedded powder (SH-2 and SH-3) and the coatings with lower surface roughness (reference sphere and SH-1). This fact underlines the influence of the rough-

Table 2: Properties of the manufactured SH coatings. λ, root-mean-square surface roughness. ϑ_s, static contact angle. ϑ_r, roll-off angle. The reported uncertainties represent the 95% confidence level. The ϑ_s and ϑ_r values are shown for the two extreme cases of pure water (G000 mixture) and pure glycerol (G100 mixture).

		SH-1	SH-2	SH-3
G000	λ, [μm]	25 ± 4	74 ± 12	142 ± 23
	ϑ_s, [deg.]	160.7 ± 2.8	150.1 ± 3.0	145.7 ± 2.0
	ϑ_r, [deg.]	1.6 ± 0.2	2.4 ± 1.0	5.4 ± 3.2
G100	ϑ_s, [deg.]	156.4 ± 5.8	147.3 ± 7.6	136.7 ± 12.0
	ϑ_r, [deg.]	2.6 ± 0.8	2.3 ± 0.8	5.4 ± 2.6

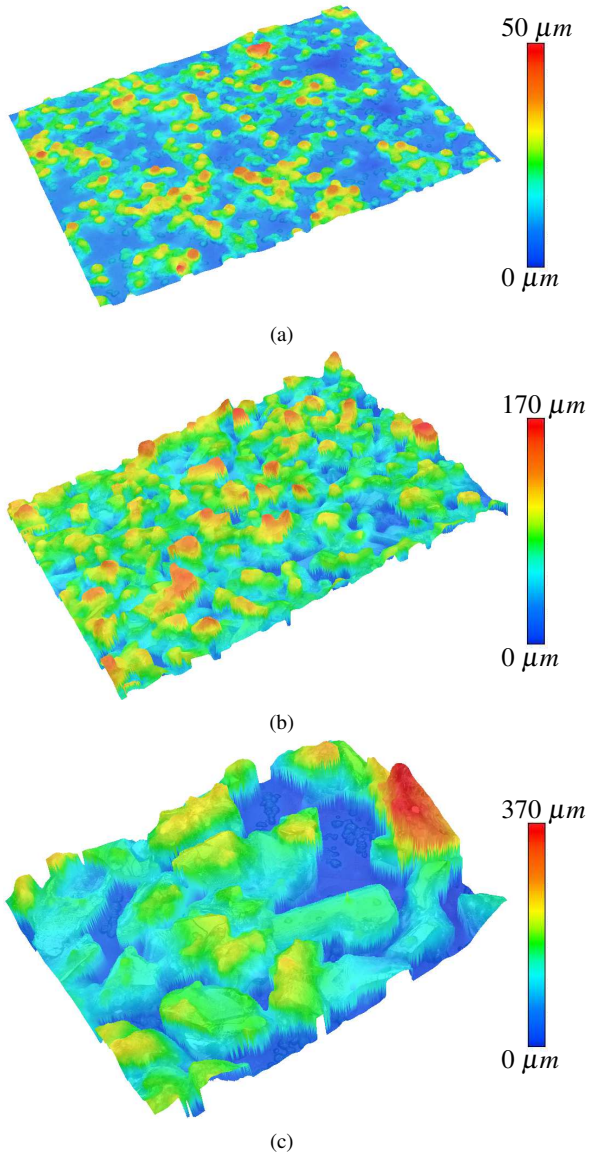

Figure 3: Digital microscopy analysis of a portion ($1.5 \times 1.0\ mm^2$) of a flat plate covered with a SH coating. (a), SH-1. (b), SH-2. (c), SH-3. The color scales indicate the range of surface roughness per each coating. All the coatings result into a random spatial distribution of the roughness elements.

Table 3: Terminal Reynolds number Re_∞ achieved by the falling spheres in the intermediate glycerol-water mixtures. An average value among all the investigated coatings is reported per each diameter and mixture.

d, [mm]	G080	G070	G060
5	25	100	290
8	65	250	680
10	110	390	1030

ness size of SH coatings on the transition process. However, all the coatings tend towards the same $V_{tr}^\star$ value at the end of the test. This behaviour has a slight influence on the normalised vertical velocity $V_z^\star = V_z/V_0$, where the profiles differ in the $t^\star \approx 10$ region, but do not show substantial variations once terminal conditions are reached. In fact, the variations of the terminal drag coefficient, evaluated as $C_{D\infty} = 3/4V_\infty^{\star 2}$ (Mordant & Pinton, 2000), were limited in the range $\pm 5\%$ for the SH coatings with respect to the corresponding reference sphere. This is in contrast with the results previously shown in Castagna *et al.* (2018) in the pure water case at much higher Re_∞, where variations of $\mathcal{O}(10^1)$ were evaluated.

One possible explanation of the influence of SH coatings on the onset of transversal motion is given by taking a closer look to the phenomena happening in the near-wall region. A sequence of images taken during the drop of a $d = 10\ mm$ SH-3 sphere in the G070 mixture is shown in Fig. 6. This sphere was taken as an example of the phenomena detected for spheres falling in the Reynolds number region where transitions of the wake occurred (see Tab. 3). These images clearly show that the air layer initially trapped among the roughness elements tends to interact with the flow around the falling object, by deforming and moving around the rear-side of the sphere. In fact, while no significant deformation is detectable in Fig. 6a, the macroscopic deformed air pocket is clearly visible in both Figs. 6b and 6c, while in Fig. 6d it turned towards the non-visible region of the sphere and shifted even more in the rear-side of the sphere. The described phenomenon is quite rapid, since less than 100 *ms* elapsed from Fig. 6a to Fig. 6d. This scenario thus suggests an interconnection between the flow develop-

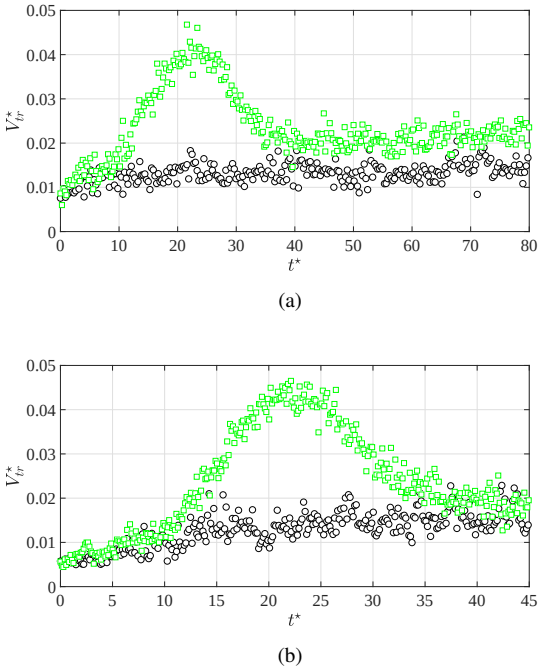

Figure 4: Non-dimensional transversal velocity $V_{tr}^\star$ time evolution: (a) $d = 10$ mm for the mixture G080, (b) $d = 5$ mm for the mixture G070. ○, reference (smooth) sphere, □, SH-3 coating. For the sake of clarity, one point out of five is reported.

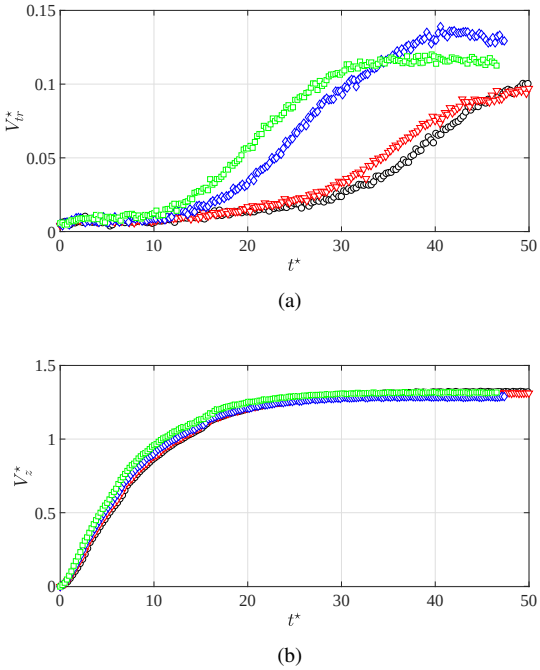

Figure 5: Non-dimensional velocities time evolution for the $d = 8$ *mm* spheres falling in the mixture G070: (a) transversal velocity $V_{tr}^\star$, (b) vertical velocity $V_z^\star$. ○, reference (smooth) sphere, ▽, SH-1 coating, ◇, SH-2 coating, □, SH-3 coating. For the sake of clarity, one point out of three is reported.

ing around the falling sphere and the air layer behaviour. In fact, the deformed air pocket is detected only in the rear-side of the falling sphere, that is the region where the laminar boundary layer underwent separation and transition to turbulence (Taneda, 1956). As introduced in Castagna *et al.* (2018), we can thus speculate that the pressure jump due to flow separation could promote the partial suction of the air layer initially trapped among the roughness elements, with a possible feedback influence on the wake development and therefore on the onset of the transversal motion. The fundamental steps of this interaction are resumed in Fig. 7: the pressure gradient developing around the falling sphere due to the separation of the laminar boundary layer and transition to turbulence determines a deformation and a movement of the air layer initially trapped in the surface roughness. This modification of the state of the sphere boundary could influence the mechanism of vorticity production at the wall. Since the latter is intimately connected to the vorticity released in the wake and therefore to the wake/path instabilities onset (Mougin & Magnaudet, 2002), a modification of the pressure gradient around the sphere could occur. This feedback loop impacts the onset of the transversal motion in the Re_∞ range analysed in this study, with a non-significant effect on the terminal drag. However, as was shown in Castagna *et al.* (2018), an increase of the falling velocity in the pure water case ($Re_\infty \gtrsim \mathcal{O}(10^3)$) determined a strengthening of the proposed mechanism with important effects also on the evaluated terminal drag, which could lead to $C_{D\infty}$ increase or decrease depending on the relative deformation of the air layer.

CONCLUSIONS

In this experimental study, the behaviour of free-falling super-hydrophobic spheres over a wide range of Reynolds number was investigated. The coatings were produced via a spray method that is adapted to macroscopic applications. The surface roughness was handled by embedding micron-sized powders and the resulting properties of the coatings were tested via three-dimensional digital microscopy. Digital goniometry analysis let us test the super-hydrophobic behaviour as a function of the considered liquid, highlighting a slight influence of the latter under the investigated operating conditions. The influence of the super-hydrophobic coatings on the onset of wake instabilities was analysed. The results pointed out a significant influence of the coatings on the onset of transversal motion for the sphere that reached a Reynolds number in the range where wake transitions occur. In this regime, a macroscopic deformation and motion of the air layer initially trapped among the surface roughness elements was detected. This phenomenon could lead to the evidenced earlier onset of path instability. A possible mechanism that connected the flow around the sphere with the behaviour of the air layer was therefore proposed.

Some of this results will be presented in the symposium.

Acknowledgments This work was supported by the Direction Générale de l'Armement (DGA), Ministère de la Défense, République Française and the Agence Nationale de la Recherche (ANR) through the Investissements d'Avenir Program under the Labex CAPRYSSES Project (ANR-11-LABX-0006-01).

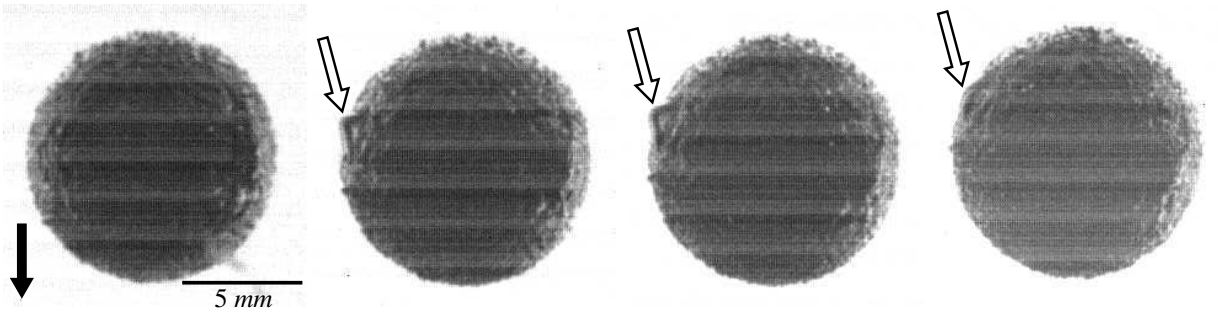

(a) $t = \bar{t}$ (b) $t = \bar{t} + 52\ ms$ (c) $t = \bar{t} + 68\ ms$ (d) $t = \bar{t} + 96\ ms$

Figure 6: Frames sampled during the drop of a $d = 10\ mm$ SH-3 sphere in the G070 mixture illustrating the motion and the deformation of the air layer (indicated by white arrows). The black arrow represents the gravity direction. The variable $\bar{t}$ designates a randomly chosen time origin.

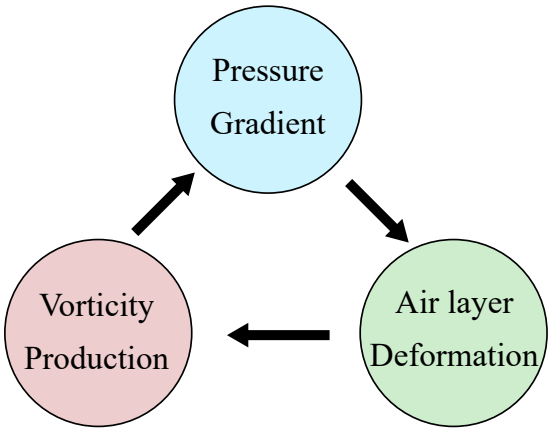

Figure 7: Schematic of a possible interaction mechanism between flow and air layer.

REFERENCES

Ahmmed, K. M. T., Patience, C. & Kietzig, A.-M. 2016 Internal and external flow over laser-textured superhydrophobic polytetrafluoroethylene (PTFE). *ACS Appl. Mater. Interfaces* **8**, 27411–27419.

Byon, C., Nam, Y., Kim, S. J. & Ju, Y. S. 2010 Drag reduction in stokes flows over spheres with nanostructured superhydrophilic surfaces. *J. Appl. Phys.* **107**, 066102.

Castagna, M., Mazellier, N. & Kourta, A. 2018 Wake of super-hydrophobic falling spheres: influence of the air layer deformation. *J. Fluid Mech.* **850**, 646–673.

Castagna, M., Mazellier, N., Passaggia, P.-Y. & Kourta, A. 2019 Modelling the influence of roughness distribution on the effectiveness of super-hydrophobic coatings in laminar flows: a porous medium approach. *Phys. Rev. Fluids* **Submitted**.

Di Felice, R. 1996 A relationship for the wall effect on the settling velocity of a sphere at any flow regime. *Int. J. Multiphase Flow* **22** (3), 527–533.

Epps, B. & Truscott, T. T. 2010 Evaluating derivatives of experimental data using smoothing splines. *Mathematical Methods in Engineering International Symposium, IPC, Coimbra, Portugal* pp. 29–38.

Ern, P., Risso, F., Fabre, D. & Magnaudet, J. 2012 Wake-induced oscillatory paths of bodies freely rising or falling in fluids. *Annu. Rev. Fluid Mech.* **44**, 97–121.

Jenny, M., Dušek, J. & Bouchet, G. 2004 Instabilities and transition of a sphere falling or ascending freely in a Newtonian fluid. *J. Fluid Mech.* **508**, 201–239.

Lapple, C. E. & Sheperd, C. B. 1940 Calculation of particle trajectories. *Ind. Eng. Chem.* **32**, 605–617.

McHale, G., Shirtcliffe, N. J., Evans, C. R. & Newton, M. I. 2009 Terminal velocity and drag reduction measurements on superhydrophobic spheres. *Appl. Phys. Lett.* **94**, 064104.

Mordant, N. & Pinton, J.-F. 2000 Velocity measurement of a settling sphere. *Eur. Phys. J. B* **18**, 343–352.

Mougin, G. & Magnaudet, J. 2002 Path instability of a rising bubble. *Phys. Rev. Lett.* **88** (1), 014502.

Raffel, M., Willert, C., Wereley, S. & Kompenhans, J. 2007 *Particle Image Velocimetry*. Springer.

Song, D., Song, B., Hu, H., Du, X., Du, P., Choi, C.-H. & Rothstein, J. P. 2018 Effect of a surface tension gradient on the slip flow along a superhydrophobic air-water interface. *Phys. Rev. Fluids* **3**, 033303.

Taneda, S. 1956 Experimental investigation of the wake behind a sphere at very low Reynolds number. *J. Phys. Soc. Japan* **11** (10), 1104–1108.

Vakarelski, I. U., Chan, D. Y. C. & Thoroddsen, S. T. 2014 Leidenfrost vapour layer moderation of the drag crisis and trajectories of superhydrophobic and hydrophilic spheres falling in water. *Soft Matter* **10** (31), 5662–5668.

Zhang, X., Shi, F., Niu, J., Jiang, Y. & Wang, Z. 2008 Superhydrophobic surfaces: from structural control to functional application. *J. Mater. Chem* **18**, 621–633.